1992ApJ...392..289R

THE ASTROPHYSICAL JOURNAL, 392:289–299, 1992 June 10

ZODIACAL EMISSION. III. DUST NEAR THE ASTEROID BELT

WILLIAM T. REACH[1]
Astronomy Department, University of California, Berkeley
Received 1991 July 25; accepted 1991 December 16

ABSTRACT

Properties of the zodiacal dust bands are derived from fits to *Infrared Astronomical Satellite* profiles of the ecliptic. Three observations lead to the conclusion that the dust-band material is spread over a range of heliocentric distances between the asteroid belt and the Sun: parallax, color temperature, and wavelength dependence of the band latitudes. The orientations of the midplanes of the bands are found to be typical of asteroids. A model of "migrating bands," wherein dust is produced near the asteroid belt and spirals into the Sun under the influence of Poynting-Robertson drag, is used to explain the range of heliocentric distances of dust-band material.

Subject headings: dust, extinction — interplanetary medium — meteoroids — minor planets

1. INTRODUCTION

Both comets and asteroids contribute solid material to the interplanetary medium, but it is not yet clear whether one source produces the bulk of the material. While the asteroidal origins of many meteorites have been inferred from mineralogical evidence and comparison to asteroidal spectra (Wetherill & Chapman 1988), the small number and severe selection effects (specifically, Earth-crossing orbits and large size) do not readily allow extrapolation to all meteoroids. Similarly, the cometary origin of many meteors, determined through their orbital elements derived by time-lapse photography and radar (Ceplecha 1987; and Sekanina & Southworth 1975), are severely influenced by selection effects (Earth-crossing orbits and high encounter velocity). Analysis of interplanetary dust particles collected in the stratosphere (Sandford 1987) and the polar ice caps (Maurette et al. 1987) has revealed evidence for both cometary and asteroidal dust, but once again selection effects (Earth-crossing orbits and low encounter velocity) make it difficult to determine whether the bulk of the dust is cometary or asteroidal. In this paper we analyze the *Infrared Astronomical Satellite* (*IRAS*) observations of the diffuse infrared background in order to determine the extent to which the asteroids are a source of interplanetary dust. Asteroids and comets probably contribute different fractions of material with different sizes. In this paper we concentrate only on particles that dominate the infrared emission (20–200 μm; Reach 1988, hereafter Paper I).

There must be a source of interplanetary dust grains, because their lifetimes are short. Poynting-Robertson drag causes the particles that produce the zodiacal light to spiral into the Sun at a rate that increases inversely with heliocentric distance (Wyatt & Whipple 1950); the time for a particle with radius $s > 1$ μm to spiral from the Earth's orbit into the Sun is $\sim 400/\beta$ yr, where $\beta \simeq 0.2/s$ (μm) is the ratio of solar radiation pressure to gravity for particles with density 2.5 g cm^{-3} (Burns, Lamy, & Soter 1979). The particles that produce the bulk of the infrared zodiacal emission and visible zodiacal light are ~ 40 μm in radius (Paper I). The Poynting-Robertson lifetimes of such particles are of order 7×10^5 yr, in agreement with solar flare exposure ages of collected interplanetary dust particles (Sandford 1986). Thus the inner solar system would be rapidly depleted of dust without a continuing, or very recent, source. Further, if the source of dust is exterior to the Earth's orbit, then a steady-state distribution, with the number density increasing inversely with heliocentric distance, will be rapidly established. Particles in the 20–200 μm size range are being continuously produced as fragments in meteoroid collisions; indeed, collisional models indicate that the number density of small particles may be *increasing* with time, while the number density of larger particles may be *decreasing* with time near the Earth (Grün et al. 1985)—an arrangement that could not last indefinitely. The relationship between the size distribution observed near the Earth, the solar system distribution of interplanetary grains, and the source region of the dust is sufficiently complicated that it has not yet been possible to disentangle the most likely origins—asteroidal or cometary—of the dust.

With the discovery by *IRAS* of extensive dust trails, related to comets (Sykes et al. 1986), and the dust bands (Low et al. 1984), related to asteroid families (Dermott et al. 1984), it became possible to study the origin of interplanetary meteoroids by direct observation of the source regions. Comets have been known to produce large meteoroids ever since the parent comet (P/Tempel) of the Leonid meteor shower was discovered in 1866. The separation of cometary ejecta into a plasma tail and a dust tail demonstrated that comets produce small particles whose orbits are affected by radiation pressure. The distribution of particles in the coma of P/Halley was determined by spacecraft during the most recent passage of the comet through the inner solar system (McDonnell et al. 1987; Mazets et al. 1986), and meteoroids were detected out to at least 250,000 km from the nucleus. The dust mass-loss rate for P/Halley, in particles smaller than 10 μm radius, was observed to be 3×10^5 g s^{-1} (McDonnell et al. 1987). Larger particles ejected into dust trails are probably the principal mass-loss mechanism for comets (Sykes & Walker 1992), so an appreciable fraction of the mass of old comets is in the form of dust trail particles.

From *IRAS* observations, it is now known that particles extend over a significant fraction of the orbit of several comets—most notably comet P/Tempel 2, whose dust trail was detected over 60° of mean anomaly (Sykes, Lien, & Walker 1990). But the comet dust trails are very sharp (angular widths

---

[1] Postal address: Code 685, NASA/Goddard Space Flight Center, Greenbelt, MD 20771.

$\lesssim 3'$), and they do not correspond to broad structures in the infrared background, so the connection between the cometary meteoroids and the more diffuse interplanetary dust complex must be indirect or evolves very rapidly. The "type 2" dust trails (Sykes 1988) are extended structures that may connect smoothly to the diffuse infrared background. However, even though the surface brightness of the type 2 trails is only a factor of a few smaller than that of the bands, the total flux—and hence the mass of dust—is much smaller for the trails than the dust bands, which extend across the entire sky.

The asteroidal dust bands are clearly extended, and they contain a substantial fraction of all of the dust in the asteroid belt (Reach 1991b). Further, the ratio of the volume density of infrared-emitting particles in the bands to that of particles near the Earth's orbit is nearly equal to the inverse ratio of the heliocentric distances, as would be established in the steady state if the dust is transported by Poynting-Robertson drag (Reach 1991b). If the density decreases as the inverse of heliocentric distance out to some maximum distance, R, then the dust was produced at, or beyond, R. Thus the source of interplanetary dust is likely to be at or beyond the asteroid belt. If the association between the asteroid families and the dust bands is correct (see Sykes et al. 1989, and Sykes 1990 for critical discussions of the origin of the dust bands), then an asteroidal origin (predominantly in the dust bands) for the bulk of the 20–200 μm interplanetary dust particles is likely.

In this paper we present a new analysis of the connection between the asteroid belt and the interplanetary dust complex. Using *IRAS* low-resolution (0°.5) scans of the ecliptic at wavelengths of 12, 25, 60, and 100 μm, we have measured the brightness and width of the dust bands for all available viewing geometries. The dust bands are clearly resolved, with widths of several degrees. Previously, the dust bands have been studied after the broad zodiacal emission has been removed via a median filter or local surface subtraction (Sykes 1990) or Fourier decomposition (Dermott et al. 1988). Analysis of unfiltered high-resolution (2′) images of the inner dust bands reveals two sharp structures, the positions of which match with the Koronis and Themis asteroid families (Sykes 1990). It is evident from comparison of the low-resolution and high-resolution data that there is a substantial amount of emission at intermediate spatial frequencies, between the sharp dust bands and the smooth background. This emission is from material that has evolved from the dust bands, and it demonstrates the connection between asteroids and interplanetary dust near the Earth.

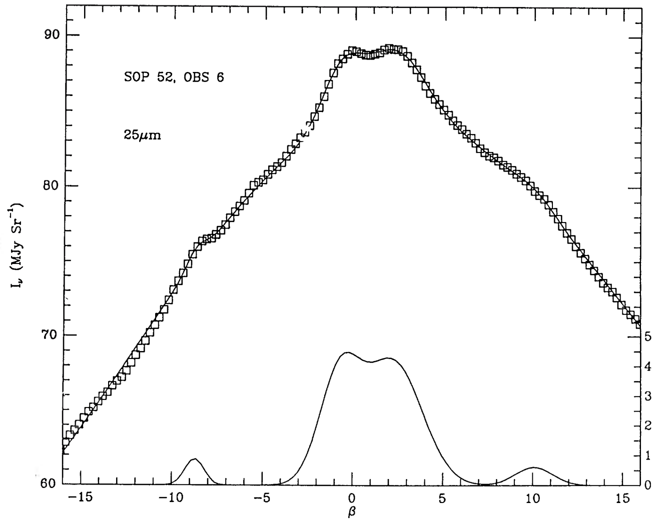

FIG. 1.—An *IRAS* profile of the ecliptic, showing the observed 25 μm surface brightness (*squares*) as a function of geocentric ecliptic latitude. The smooth line through the observations is the combined polynomial and Gaussian fit. The Gaussian portion of the fit is also shown separately (*lower curve*) on a twice-enhanced scale (*right-hand border*). The profile was made on UT date 1983.1376, with a constant solar elongation $\epsilon = 90°.7$, crossing the ecliptic at longitude $\lambda = 240°.2$.

2. SEPARATION OF ASTEROIDAL AND LOCAL DUST

The most distinctive features of the dust bands are their shapes and spectra. In this section we present a method of separating the bands from the much brighter and smoother emission of local dust using their shapes. The data used are the 0°.5 resolution, 0°.25 sampled profiles of the ecliptic made by the *IRAS*. These profiles are contained in the Zodiacal Observation History File (version 2; cf. *IRAS* Explanatory Supplement 1988); a typical profile is shown in Figure 1. The bands are evident as "bumps" at latitudes of approximately ±10° and ±1°.4 with respect to a mean ecliptic latitude of +0°.8. These will be referred to as the "outer" and "inner" band pairs, respectively. There are four well-detected bands, two for each major band pair, in each profile of the ecliptic. Since the variations with observation date and orientation of the separation and mean latitudes of the two bands of a band pair contain information about their distance and midplane (as discussed in the following sections), we fit the northern and southern components of a band pair independently. Further, the observed location of the bands depends on the wavelength of emission, so we fit scans in different *IRAS* bands independently.

The band peaks are well fitted by Gaussians, with the smooth zodiacal emission fit by a fourth-order polynomial baseline within 16° of the ecliptic. There is a total of 18 free parameters for each profile of the ecliptic: five for the baseline, three each for the four Gaussians, and a coefficient of the H I column density (Heiles & Habing 1974; Cleary, Haslam, & Heiles 1979) to represent the high-latitude Galactic infrared emission (Boulanger & Perault 1988). No $|\beta| < 16°$ scans passing within 10° of the Galactic plane were used, due to the strong fluctuations in the infrared background there. Even at high galactic latitudes, fluctuations in the Galactic 100 μm emission dominate the zodiacal dust bands so that we could not use our fitting scheme reliably for the 100 μm data. In the actual fitting scheme, the number of detectable Gaussians in a profile was reduced whenever a strong point source, or an anomalous Galactic feature poorly fitted by the H I map, was present within the expected domain (central latitude ± average width) of a band. Features sharper than 1° and brighter than 1 MJy/sr^{-1} were deemed anomalous. Profiles at 12 μm were most strongly affected by this procedure, because the number of point sources that dominate over the background brightness is much larger than at longer infrared wavelengths. There are 867 profiles with fits for all four Gaussians at 25 μm and 60 μm, and 190 profiles with fits at 12 μm, 25 μm, and 60 μm. In Table 1, the mean amplitude, center, and width of the bands are summarized for the three wavelengths. For each quantity, the range of values obtained in the fits are indicated after the "±." (For the peak latitudes of the bands, the annual and parallactic variations were subtracted before calculating the range.) The statistical measurement uncertainties are substantially smaller than the range of observed values; systematic effects, both real

TABLE 1

Gaussian Properties of the Dust Bands

Band	12 μm	25 μm	60 μm
A. Peak Surface Brightness (mJy sr^{-1})			
N outer	0.4 ± 0.2	1.1 ± 0.5	0.8 ± 0.4
N inner	1.1 ± 0.5	3.0 ± 1.0	1.5 ± 0.5
S inner	1.4 ± 0.3	2.9 ± 1.2	1.6 ± 0.6
S outer	0.6 ± 0.3	0.8 ± 0.3	0.7 ± 0.4
B. Geocentric Latitude of Peak			
N outer	9°.7 ± 0°.1	9°.6 ± 0°.1	9°.6 ± 0°.2
N inner	1.4 ± 0.1	1.4 ± 0.1	1.4 ± 0.1
S inner	−1.4 ± 0.1	−1.4 ± 0.1	−1.4 ± 0.1
S outer	−9.7 ± 0.1	−9.6 ± 0.1	−9.6 ± 0.1
C. Full Width at Half-Maximum Brightness			
N outer	3°.3 ± 1°.3	3°.7 ± 1°.1	3°.2 ± 1°.5
N inner	3.3 ± 1.1	3.3 ± 1.2	3.2 ± 1.2
S inner	3.7 ± 1.3	3.3 ± 1.2	3.4 ± 1.4
S outer	2.8 ± 1.1	3.1 ± 0.8	3.0 ± 1.4

and false (from the fitting method), dominate the quoted ranges.

In order to determine the wavelength dependence of the band properties, we analyzed the differences and ratios of band properties obtained from simultaneous scans (at different wavelengths). The mean ⟨12 − 25⟩ and ⟨60 − 25⟩ differences between the band separations and widths were found to be statistically significant (using the paired *t*-test). For the outer band pair, the separation between the northern and southern components is 4.1% ± 0.7% larger at 12 μm wavelength compared to 60 μm wavelength. The sense of the wavelength-dependence is such that the bands are wider, *and* the separations between northern and southern components of a band pair are greater, at shorter wavelengths. This would be the case, for example, if the emitting region has a gradient in temperature, such that the warmer material is closer to the Sun. The relationship between heliocentric and geocentric latitude is illustrated in Figure 2. One may show that the fractional shift $\delta\beta$ of the band-pair separation $\Delta\beta$ is related to the fractional shift δR in the radius of the band pair as $\delta\beta/\beta = -\delta R/R(R^2 - 1)$. If the radius of the 60 μm emitting region is 2.5 AU, then the radius of the 12 μm emitting region is 2.0 AU.

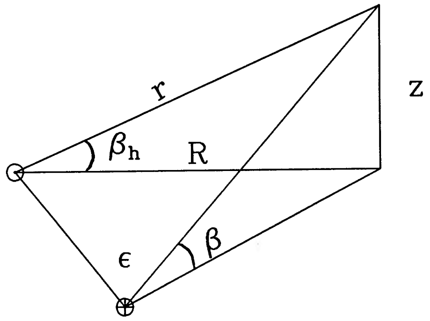

Fig. 2.—Schematic illustration of the relationship between heliocentric latitude, β_h, and geocentric latitude, β, for an object at heliocentric distance, R, and altitude, z. An object that moves closer to the Sun, at constant heliocentric latitude, is seen from the Earth at a higher geocentric latitude.

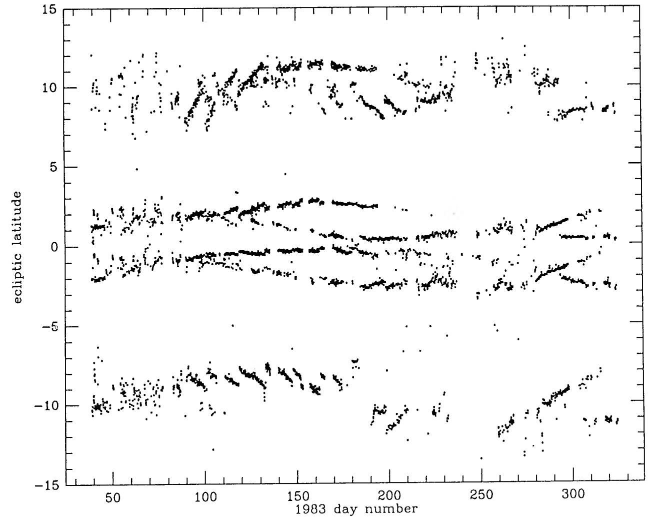

Fig. 3.—Ecliptic latitude of the peak brightness of the dust bands, plotted as a function of the observation date. The annual modulation of the latitudes is due to the tilt of the band-pair midplanes with respect to the ecliptic; when the Earth was above the band-pair midplanes, they were observed at negative ecliptic latitude. The annual variation breaks into two sinusoidal variations for each band, because lines of sight leading and trailing the Earth (observing opposite celestial hemispheres) were observed on opposite halves of each *IRAS* orbit.

3. GEOMETRY OF THE DUST BANDS

The latitudes of peak brightness of the dust bands as derived from the Gaussian fits are shown in Figure 3 as a function of observation date, and in Figure 4 as a function of ecliptic longitude. The symmetries between the northern and southern components of the outer and inner band pairs are clear, as well as the following trends. First, there is a sinusoidal annual variation of the band latitudes, with the northern and southern components of a band pair oscillating, *in phase*, about their mean position, maintaining roughly constant separation. (For each band, there are two sinusoidal variations in Fig. 3,

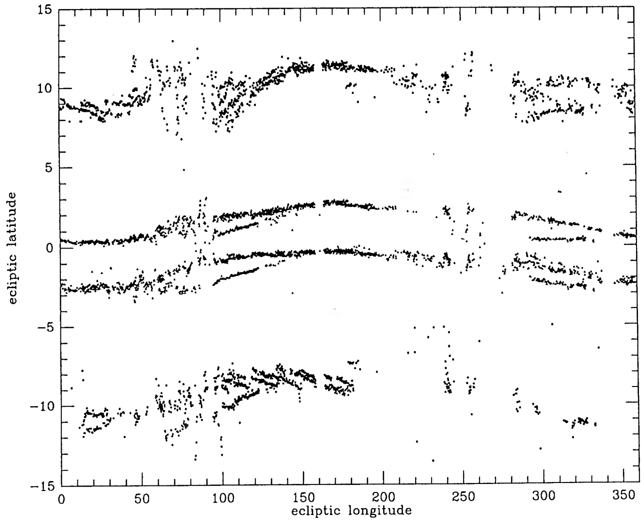

Fig. 4.—Ecliptic latitude of the peak brightness of the dust bands, plotted as a function of the geocentric longitude of the line of sight. The expected sinusoidal variation is evident but confused, since the Earth moved around the Sun during the *IRAS* observing lifetime, and since the solar elongation of the line of sight was modulated with an approximately monthly timescale.

because scans "leading" and "trailing" the Earth in its orbit observed areas on opposite sides of the sky.) Second, there is a "sawtooth" pattern (Fig. 3) superposed on the annual variation, in which the northern and southern components of a band pair vary *out of phase*. These effects are combined with each other in a systematic way that may be easily disentangled, by computer if not by eye, given the *IRAS* pointing information (time, ecliptic longitude, and solar elongation) for each profile. Similar effects are seen in the variation of the latitude of peak brightness of the smooth zodiacal emission (Hauser 1988; also Reach 1991a, hereafter Paper 2), and they are well understood. The annual variation is due to the changing altitude of the Earth with respect to the midplane of the band pairs, and the "sawtooth" pattern is due to the changing solar elongation angle used in the *IRAS* program of sky mapping. These effects are used to measure the inclination and distance of the band pairs in the following subsections.

3.1. *Inclination of the Dust Bands*

Consider a simple model of the dust bands: each band pair consists of two parallel rings, with radius R, centered on the Sun, separated from each other by a distance $2z$, and inclined with respect to the ecliptic by an angle i, with midplane intersecting the ecliptic with longitude of ascending node Ω. The rings are presumed to be circular, based on the expectation that the forced eccentricities of particle orbits near the asteroid belt are small ($e_f \lesssim 0.04$; Dermott et al. 1984). The relationship between the heliocentric and geocentric latitudes of the bands are illustrated for clarity in Figure 2. The geocentric latitude of the northern band is

$$\beta_N = \tan^{-1}\left[\frac{z + R\tan i \sin(\lambda_h - \Omega)}{\cos\epsilon + \sqrt{R^2 - \sin^2\epsilon}}\right], \qquad (1)$$

and the geocentric latitude of the southern band is

$$\beta_S = \tan^{-1}\left[\frac{-z + R\tan i \sin(\lambda_h - \Omega)}{\cos\epsilon + \sqrt{R^2 - \sin^2\epsilon}}\right], \qquad (2)$$

where λ_h is the heliocentric longitude at which the line of sight intersects the band, and ϵ is the solar elongation of the line of sight. The variation of the band latitude contains symmetric and asymmetric terms. The average of the latitude of the northern and southern bands is the symmetric term, a sinusoidal variation with heliocentric longitude, while the difference is (twice) the asymmetric term (discussed in the next section). If the line of sight is tangent to the Earth's orbit ($\epsilon = 90°$), as is nearly true for the majority of *IRAS* scans, then the average latitude is

$$\tan\beta = \frac{\tan\beta_N + \tan\beta_S}{2} = -\frac{R}{\sqrt{R^2 - 1}}\tan i \sin\left(\lambda - \Omega \pm \sin^{-1}\frac{1}{R}\right), \qquad (3)$$

where λ is the geocentric ecliptic longitude of the line of sight, and the upper (lower) sign in the $\pm$ refers to a line of sight that leads (trails) the Earth in its orbit. The *IRAS* profiles of the ecliptic were made at constant ϵ, and approximately constant λ at low latitudes, so equation (3) can be used to model the sinusoidal oscillations in the mean latitude. There are three model parameters (i, Ω, and R) to be determined. The phase difference, $\Delta\phi$, between the annual variation of the mean latitude for scans leading and trailing the Earth can be used, in principle, to measure the radius of the bands, since $R \simeq \sec\Delta\phi/2$ (see eq. [5] of Paper II). However, the phase differences are not sufficiently accurate to determine the band-pair distances; band distances are better measured through parallax (see next section).

The annual variation of the mean latitude determines i and Ω. For each profile with successful fits to the northern and southern component of a band pair, we determined the average latitude. Using equation (3) as a model, we found the best-fitting inclination, i, and ascending node, Ω, for each band pair. The results are shown in Table 2, together with representative values for dust near the Earth's orbit. For the smooth cloud, the tabulated heliocentric distance is the mean heliocentric distance of dust contributing to the total infrared brightness seen from the Earth (Paper II), and β_h is the half-width at half-maximum of the local dust density (Reach & Heiles 1988). The dust bands are clearly distinct from the local dust. The different Ω for the bands and the smooth cloud results from the different secular perturbations felt near the asteroid belt as opposed to near the Earth (as discussed in more detail in § 5); the similarity of the band orbital elements to those of Jupiter indicate the strong influence of the most massive planet on the dust band particle orbits (Dermott et al. 1985).

3.2. *Distances to the Dust Bands*

The distances of the dust bands from the Sun can be determined parallactically from the variation of the band-pair separation as a function of solar elongation, ϵ (the angle between the line of sight and the Sun). Lines of sight with larger ϵ intersect the bands closer to the Earth, so that the bands have a greater geocentric angular separation. Using equations (1) and (2), the separation between the two Gaussians of a band pair is

$$\Delta\tan\beta = (\tan\beta_N - \tan\beta_S) = \frac{2z}{\cos\epsilon + \sqrt{R^2 - \sin^2\epsilon}}. \qquad (4)$$

IRAS profiles covered the range $60° < \epsilon < 120°$, but successful band fits were only possible over the range $80° < \epsilon < 110°$. (Most scans at extreme elongations were made at longitudes where the Galactic plane crosses the ecliptic and were therefore excluded.) Near $\epsilon = 90°$, the first-order expansion of equation (4) is

$$\Delta\tan\beta \simeq \frac{2z}{\sqrt{R^2 - 1}}\left[1 + \frac{1}{\sqrt{R^2 - 1}}\left(\epsilon - \frac{\pi}{2}\right)\right]. \qquad (5)$$

The variation of band-pair separation with solar elongation are shown for a subset of the *IRAS* scans made between 1983 March 30 and April 13 in Figure 5. A line may be fitted through the data, and from equation (5) the ratio of the $\epsilon = 90°$ intercept to the slope is approximately $\sqrt{R^2 - 1}$. From this

TABLE 2

GEOMETRY OF THE DUST BANDS

Band	i	Ω	R_p(AU)	β_h
Outer band	1°3 ± 0°2	91° ± 2°	1.9 ± 0.2	8°2 ± 0°2
Inner band	1.1 ± 0.2	102 ± 5	1.8 ± 0.2	1.2 ± 0.1
Smooth cloud	1.3–1.7[a]	53–79[a]	1.3	14

[a] Values of i and Ω for dust near the Earth's orbit (first value; from Paper I), and for dust near the ecliptic (second value; from Paper II).

1992ApJ...392..289R

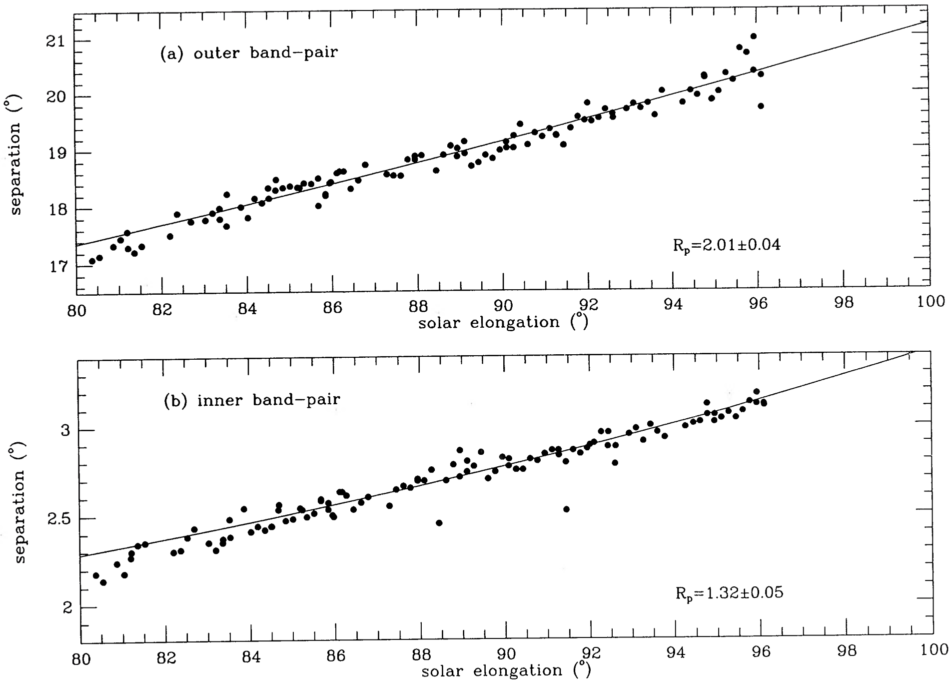

FIG. 5.—Separation between the northern and southern bands of the outer band pair (*a*), and the inner band pair (*b*), as a function of the solar elongation of the line of sight, for *IRAS* 25 μm scans made between 1983 March 30 and April 13. The separation between the northern and southern components of a band pair is greater for higher elongation lines of sight because these lines of sight intersect the bands at smaller geocentric distances. Curves through the data are least-squares fits of eq. (4), and the "parallax distance" is indicated in the lower right of each panel.

subset of *IRAS* scans, the outer band pair is 2.04 ± 0.04 AU from the Sun, and the inner band pair is 1.32 ± 0.05 AU from the Sun.

We identified several approximately month-long periods during which the *IRAS* observing strategy systematically varied the solar elongation between about 80° and 100°, and we were thus able to determine the distance to the bands at several different longitudes. The derived locations of the bands are shown as a function of heliocentric longitude in Figure 6. In Figure 7, the same data are plotted in polar form; each point has been placed according to the parallactic distance and the heliocentric longitude where the line of sight intersects the

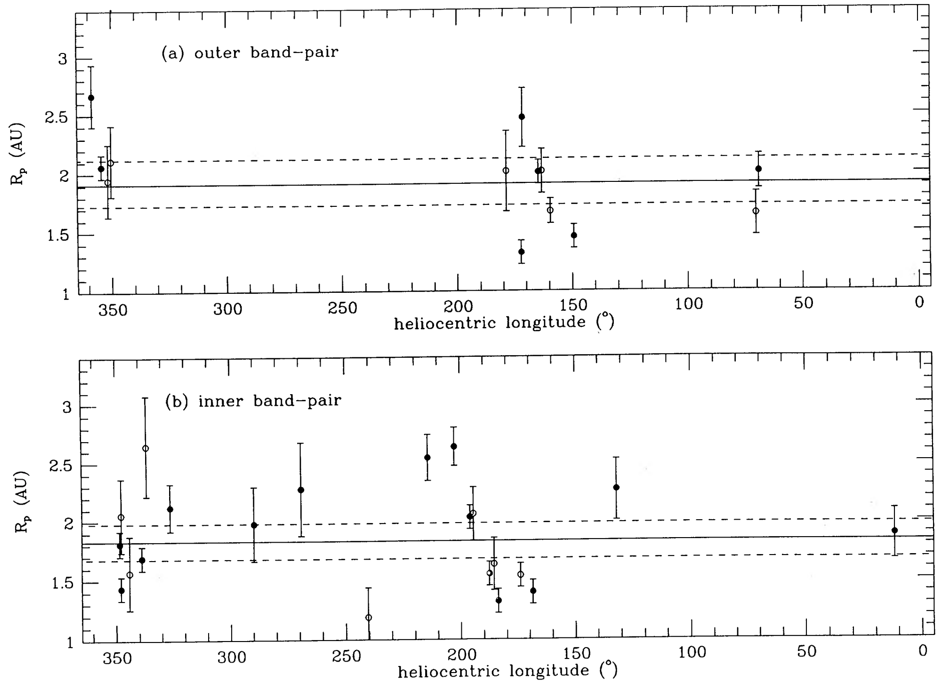

FIG. 6.—(*a*) Parallax distances of the outer band pair and (*b*) the inner band pair as determined from separate segments of the *IRAS* data base, are shown as a function of the heliocentric longitude at which the line of sight intersects the band pair. The lengths of the error bars are the uncertainties in the fits of eq. (4) to the elongation-dependence of the band-pair separation (see Fig. 5). Filled circles are derived from the 25 μm scans, and open circles are derived from 60 μm scans.

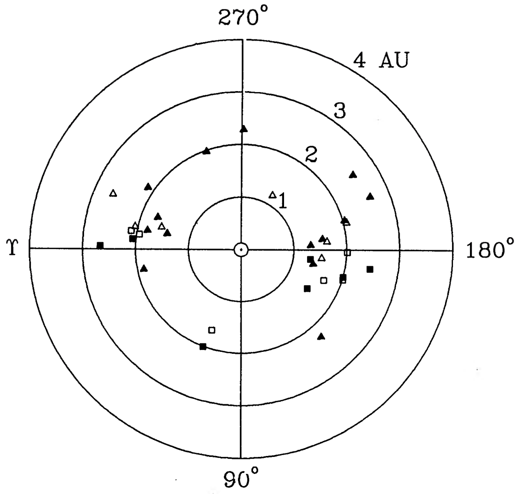

FIG. 7.—The same data as in Fig. 6 are plotted in polar form, with the Sun at the center and circles with radius 1, 2, 3, and 4 times that of the Earth's orbit shown. Both the outer band pair (*squares*) and inner band pair (*triangles*) are shown. Filled circles are derived from the 25 μm scans, and open circles are derived from 60 μm scans.

band. By connecting the points, it is possible (in principle) to determine the shape of the bands and test the hypothesis of azimuthal symmetry. If the bands were eccentric, for example, the points in Figure 7 trace an ellipse. The scatter in the data is too large to reveal the subtle forced eccentricity expected for particles influenced by Jovian perturbations ($e_f \simeq 0.04$; Dermott et al. 1988). We can set an upper limit of $e_f < 0.3$ from Figure 7*b*. The weighted mean values of R_p, the "parallactic" distances, are given in Table 2 and plotted as a straight line in Figure 6, with dashed lines indicating statistical uncertainty.

The heliocentric angular separation of the bands was derived from the geocentric separation and R_p, and the results are shown in the last column of Table 2. The heliocentric separation between the bands should correspond to the inclination of the particle orbits. The fact that we derive an inclination that is *smaller* than that of the Eos asteroid family suggests that the dust band particles are probably not associated with the entire family, but rather with the debris from collisional destruction of an asteroid with inclination that is smaller than the Eos family average. If the parent asteroid of the dust band was an Eos member, its inclination was at the lower (2 σ) limit of the distribution of family member inclinations (Sykes 1990).

4. SPECTRA OF THE DUST BANDS

The amplitudes of the Gaussians that fit the peaks of the dust bands were used to determine their 12/25 μm and 60/25 μm colors. The medians and dispersions of the color ratios are listed in Table 3. For each band pair, the blackbody color temperature that best matches the color ratios is also listed; the uncertainty in the temperature was derived from the dispersion of the color ratios together with the goodness-of-fit of a single blackbody. The temperatures are those that would be obtained by rapidly rotating blackbodies at distances from the Sun of 2.3 ± 0.3 AU (outer band pair) and 1.8 ± 0.2 AU (inner band pair). The colors of the dust bands also correspond to those calculated for the grain composition and size distribution models that match the spectrum of dust near the Earth's orbit (Paper I), if the grains are heated by the solar flux at 2.3 and 1.8 AU, respectively.

TABLE 3

SPECTRUM OF THE DUST BANDS

Band	12/25	60/25	T_{bb}(K)	R_{sp}(AU)
Outer band	0.29 ± 0.06	0.68 ± 0.08	180 ± 13	2.3 ± 0.3
Inner band	0.34 ± 0.05	0.50 ± 0.06	209 ± 11	1.8 ± 0.2
Smooth cloud[a]	0.67	0.32	269	1
Asteroid belt	0.27–0.14	0.61–0.83	150–180	2.3–3.2

[a] Values of 12/25 and 60/25 colors (Paper I) and the blackbody color temperature (Paper II) refer to dust near the Earth's orbit; the total brightness observed along a line of sight at $\epsilon > 90°$ has a somewhat cooler color temperature.

The spectrum of the inner band pair is clearly "warmer" (both higher 12/25 and lower 60/25 colors) than the outer band pair, and we infer that the dust in the inner band pair is *closer to the Sun*. The range of temperatures and color ratios expected from dust in the asteroid belt is shown in the last row of Table 3 for comparison. The dust in both band pairs is warmer than would be expected if the dust were distributed within their parent asteroid families. This conclusion is in agreement with the parallactic distances derived in the previous section and indicates that dust has migrated inward from the asteroid belt.

5. INTERPRETATION

The parallactic (§ 3.2) and spectroscopic (§ 4) distances of the extended band pairs are both smaller than the distance to the asteroid belt. In contrast, when viewed at high resolution, bands are seen which are located in the asteroid belt (Sykes 1990). Thus, material in these bands is distributed along large ranges of heliocentric distance. We therefore conclude that the material migrates inward from the asteroid belt, where it is produced. The physical mechanism for such migration is Poynting-Robertson drag. In this section we derive a model for the dust bands that includes migration of the material from its site of formation. The model is a step toward understanding the putative connection between the asteroids and the interplanetary dust complex.

5.1. *Formation of the Dust Bands*

We consider the following scenarios for production of the dust in the asteroid belt: recent catastrophic disruption of a single ~15 km asteroid (Sykes & Greenberg 1986) or comet, and comminution of debris left over from the formation of the major Hirayama families (Sykes et al. 1989). If the Hirayama families formed as a result of catastrophic disruption of an asteroid (Gradie, Chapman, & Williams 1979), then the difference between these scenarios is only the size of the parent asteroid and the time elapsed since its destruction. Both scenarios are able to explain the dust bands, but they provide a somewhat different context for interpretation of the observations.

Suppose that an asteroid is catastrophically disrupted in the asteroid belt. The collision imparts some kinetic energy to the fragments of the asteroid, and if this energy exceeds the gravitational binding energy, then the fragments disperse. For a collision that disrupts an asteroid larger than a few kilometers in diameter, the kinetic energy may not be sufficient to disperse the fragments, and a gravitationally bound "rubble pile" results (Davis et al. 1985). For collisions that do impart sufficient kinetic energy to the fragments that they can disperse, the excess kinetic energy is likely to be small compared to the orbital energy. Thus the fragments retain essentially the same orbit as the parent asteroid (which no longer exists), with some small dispersions in orbital elements. The orbits precess due to Jovian perturbations, and the orbital nodes spread across all longitudes after $\sim 10^7$ yr (Sykes & Greenberg 1986). At this time, the fragments occupy a toroidal volume bounded vertically by the inclination of the parent asteroid and bounded radially by the perihelion and aphelion of the parent object. Because the particles spend more time near the extrema of their vertical motion, the torus is effectively edge-brightened. There are significant enhancements in the particle density near the perihelion and aphelion of the particle orbits. (See Sykes 1990 for illustration and mathematical form of the dust torus.) The appearance of the dust torus to an observer on the Earth is two parallel bands (a band pair) stretching across the sky.

Suppose now that the formation of the asteroid families produced debris with a range of sizes, including both the observed family members and smaller fragments. Let us define a critical fragment size, below which the time scale for mutual collisions is shorter than the time since the destruction of the parent asteroid of the family. If a significant fraction of the parent asteroid is converted into fragments smaller than the critical size, then mutual collisions among fragments will create dust. The theoretical equilibrium size distribution, obtained by balancing collisional gains and losses, is a power law of the form $dn/dm \propto m^{-\alpha}$, where $\alpha = 11/6$ (Dohnanyi 1970). The evolution of the dust size distribution and the fading of a dust torus as it ages was modeled by Sykes & Greenberg (1986).

Whether the dust we observe is the result of the formation of the asteroid family, or the relatively recent disruption of a family member, we obtain essentially the same initial distribution of material in the asteroid belt. The only significant difference in the predicted current appearance of the bands is that under the second hypothesis (debris left over from family creation), the orbital elements of the dust band particles are related to the parent body of the entire asteroid family, while under the first hypothesis (recent asteroid collision), the orbital elements are related to those of a smaller asteroid that no longer exists. Thus if the orbital elements of the band material are not the same as those of the known family members, the second hypothesis is unlikely. Agreement of the band orbital elements with those of the family members does not necessarily rule out the first hypothesis, since the recent asteroid collision may have involved a family member.

It was originally proposed (Dermott et al. 1984) that the outer and inner band pairs were associated with the two largest Hirayama families of asteroids due to the agreement of the band latitudes and the mean inclination of family member orbits. Since then, it has been shown (Sykes 1990) that the observed latitudes of the α, β, and γ bands are consistent with the orbital elements of the members of the Themis, Koronis, and Eos families, respectively. (In the low-resolution data, the α and β bands merge into the inner bands; the γ band is the same as the outer band.) In order to match the location of the bands to the asteroid families, Sykes (1990) increased the dispersions of the dust orbital elements by a factor of ~ 2 over the dispersions among known family members. It is reasonable that the dust orbital elements have larger dispersion than the family members, because kinetic energy is imparted to them in mutual fragment collisions. The apparent agreement of the band latitudes with the predictions based on the family orbital elements is good evidence that the dust was produced by comminution of debris left over from the formation of the asteroid families (Sykes 1990).

5.2. *Migrating Band Model*

Once there is a distribution of debris smaller than ~ 1 cm, whether left over from an ancient event or produced in a recent collision, the surface area of the debris is much larger than the surface area of the parent body. Since we preferentially observe the smaller particles, their evolution is important for interpretation of the properties of the observed dust bands. Two processes dominate the evolution of the dust: collisional comminution and radiation pressure. Mutual collisions tend to drive the size distribution of the dust into collisional equilibrium, while radiation drag removes smaller particles. Particles between ~ 0.1 μm and 1 μm in radius are actually ejected from the solar system, due to radiation pressure (Burns et al. 1979). More importantly, larger particles are transported *inward* from the site of production to the Sun due to the nonradial component of solar radiation pressure in the rest frame of the orbiting particle (Poynting-Robertson drag; see, e.g., Wyatt & Whipple 1950). The time for a particle, 40 μm in radius and produced in the asteroid belt, to spiral into the Sun is 7×10^5 yr. The time for the orbital nodes of the debris from and asteroid collision to be spread over all longitudes is 10^6–10^7 yr (Sykes & Greenberg 1986). Thus any dust smaller than ~ 100 μm radius would spiral into the Sun before Jovian perturbations could precess its orbit sufficiently to form a complete dust band. Further, smaller fragments produced in mutual collisions among band-pair particles must have already spiraled past the Earth and into the Sun. Thus the dust bands are rapidly depleted of the small particles that are believed to produce the infrared emission.

Dust that is removed from the production site by radiation drag is replaced by fragments from mutual collisions among larger fragments still at the production site. Thus there is a continuous production of fragments that are transported inward by radiation drag, and an equilibrium number density in the source region that depends on the production rate. Consider the distribution of this dust that is "migrating" inward from its site of production. Suppose the particles start with a specified (e.g., Gaussian) distribution of orbital inclinations, a random distribution of orbital nodes, and low eccentricities. The distribution of semimajor axes is initially centered on the site of production, but rapidly evolves due to radiation drag. The continuity equation for the distribution of orbital semimajor axes for circular orbits is (see Leinert, Röser, & Buitrago 1983)

$$\frac{1}{a^2}\frac{\partial}{\partial a}\left[a^2 n(a)\frac{da}{dt}\right] = -\frac{\partial n(a)}{\partial t} = 0\ , \tag{6}$$

where the number of particles with orbital semimajor axis in the range a to $a + da$ is defined as $n(a)da$, and the distribution of orbital inclinations is assumed to be independent of a. The right-hand side of equation (6) is set to zero because we assume that the density of particles at a specific position is constant. Since the rate of decay of semimajor axis is inversely proportional to semimajor axis (Wyatt & Whipple 1950), the steady state distribution is $n(a) \propto a^{-1}$. For comparison, inversion of zodiacal light observations by the *Helios* spaceprobe in the inner solar system revealed a particle density $n(r) \propto r^{-1.3}$ (Leinert et al. 1981), *Pioneer 10* observations between the Earth's orbit and the asteroid belt yielded $n \propto r^{-1.5}$ (Hanner et al. 1976), and *IRAS* observations have yielded $n \propto r^{-1.1}$ (Paper II). The time scale for establishing the steady state distribution is similar to the timescale for an individual particle to spiral into the Sun, so we may segregate the debris into two evolutionary classes: the large fragments that are essentially unaffected by radiation pressure since the production event, and the migrating fragments that are spiraling into the Sun. The large fragments can be observed as bands *in the asteroid belt*, while the smaller, "migrating" fragments are distributed throughout the inner solar system.

Now consider the integrated brightness of the migrating material,

$$I_\nu(\beta) = \int ds\, \mathscr{E}_\nu(r, \beta_h) \,, \tag{7}$$

where $\mathscr{E}_\nu$ is the volume emissivity, r is the distance from the Sun, β_h is the heliocentric latitude, β is the geocentric latitude, and the integral is to be performed over the line of sight. For convenience, we renormalize the volume emissivity of dust at distance r from the Sun,

$$\mathscr{E}_\nu(r, \beta_h) = \tilde{\mathscr{E}}_\nu(r, \beta_h) r^{-1} \,, \tag{8}$$

assuming the same size distribution at r as near the Earth's orbit. (The temperature dependence of the grains is included in $\tilde{\mathscr{E}}_\nu$, and the factor r^{-1} accounts for the density.) The assumption that the shape of the size distribution does not change as dust migrates from the site of production is unlikely to be exactly correct; however, only drastic changes in the size distribution, such as a significant enhancement of the fraction of grains smaller than 1 μm, could affect the infrared spectrum, and drastic changes are not expected because of the low collision rates. We have implicitly assumed that the particle orbits are circular by using r and a interchangeably; this is reasonable because asteroid family members are not very eccentric, and Poynting-Robertson drag circularizes orbits.

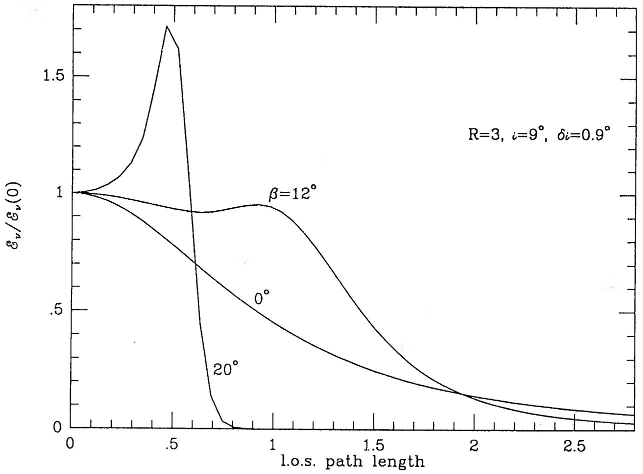

FIG. 8.—The volume emissivity along the line of sight for a "migrating band" model with radius $R = 3$ AU, inclination $i = 9°$, and dispersion $\delta i = 0\overset{\circ}{.}9$. The three curves are for lines of sight with geocentric latitudes of $\beta = 0°$, 12°, and 20°, as labeled. The low-latitude emission is produced along the line of sight, weighted toward the observer due to the heliocentric radial variation of the dust density and temperature. The intermediate-latitude emission is produced along the line of sight, but with a "bump" in between the observer and the band radius. The high-latitude emission is produced near the observer, primarily in a ring with a distance that depends on the ecliptic latitude (see text).

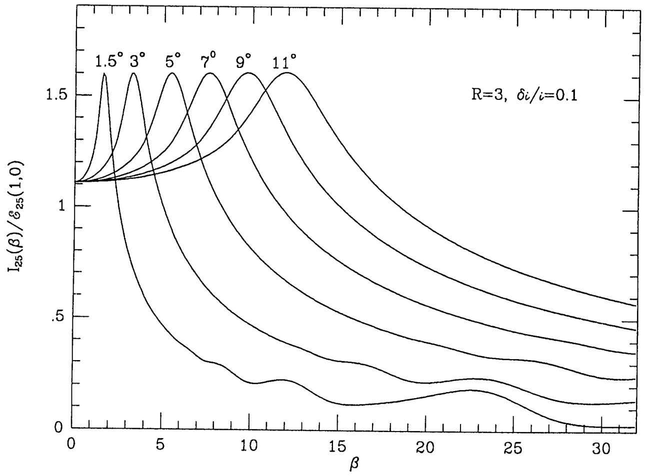

FIG. 9.—Model profiles of "migrating" bands created by particles that originate at $R = 3$ AU. Each curve corresponds to a model with a specified orbital inclination; the dispersion in inclinations is 10% for each model. The profiles show the integrated brightness, observed from the Earth at solar elongation $\epsilon = 90°$, as a function of geocentric ecliptic longitude. The brightness profiles are normalized with respect to the volume emissivity of dust near the Earth's orbit, so the scale of the vertical axis are effective path length in AU. (Wiggles in the low-inclination band models at high latitudes are due to round-off error in integrating over the tail of the inclination distribution.)

In Figure 8, the volume emissivity is shown as a function of path length along three lines of sight, for a migrating band model with outer radius $R = 3$ AU, proper inclination $i = 9°$, and inclination dispersion $\delta i = 0\overset{\circ}{.}9$. The three lines of sight have the same solar elongation, $\epsilon = 90°$, but different latitudes: $\beta = 0°$, 12°, and 20°. The low-latitude and high-latitude emission are produced relatively locally, while the intermediate-latitude emission is produced along the line of sight, with a "bump" between the observer and the band radius. The "bump" occurs when the heliocentric latitude of the line of sight is equal to the inclination of the particle orbits. For $\beta > i$, the distance along the line of sight from the observer to the bump is

$$s_b = \frac{\sin i/\sin \beta}{\sqrt{1 - (\sin i/\sin \beta)^2}} \,. \tag{9}$$

Thus a local maxiumum in the emissivity for each β (as long as $\beta > i$) occurs in a ring that is elevated above the ecliptic, as is evident from the peak in the $\beta = 20°$ curve in Figure 8. The latitude of peak emission from the bands can therefore be associated with a particular distance along the line of sight, and this distance determines the spectroscopic and parallactic distance of the bands. There is no "bump" for $\beta < i$, because the heliocentric latitude of the line of sight is always less than the inclination of the particle orbits. The low-latitude ($\beta < i$) emission is produced along the line of sight through the bands with a monotonically decreasing emissivity. Thus it is not possible to separate low-latitude emission from migrating dust from low-latitude emission from the rest of the interplanetary dust: the spectral and parallactic distances are the same.

In Figure 9, the results of integrating equation (7) over the line of sight are shown for model bands with a range of orbital inclinations from $i = 1\overset{\circ}{.}5$ to 11°; in all cases, the dispersion in the inclination distribution is 10%. The line of sight is perpendicular to the Earth's orbit ($\epsilon = 90°$), as is typical for an *IRAS* scan, and the curves show the brightness as a function of geocentric latitude. Each curve is normalized with respect to the volume emissivity at the Earth's orbit, $\mathscr{E}_\nu(1, 0)$, so the vertical axis is an effective path length. The effective path length may be

1992ApJ...392..289R

converted into a surface brightness by multiplying by $\mathscr{E}_\nu(1, 0)$ (from Paper I), and then multiplying by the density ratio between the migrating band and the total density at the Earth's orbit. The migrating dust is clearly visible at all latitudes, and models with an inclination greater than 5° do not drop to half peak brightness until $\beta > 20°$.

In Figure 10, model profiles are shown for four different wavelengths, corresponding to the *IRAS* and *COBE* mid-infrared filters. The profiles are normalized as in Figure 9. The migrating bands have a spectrum that is significantly cooler than local dust, in agreement with observations of the spectrum of the dust bands. The spectrum of the dust bands peaks between 25 μm and 60 μm, while the spectrum of dust near the Earth's orbit peaks between 12 μm and 25 μm (Paper I), and the total brightness of dust near the ecliptic peaks near 25 μm (Paper II).

Figures 8 and 10 show that migrating dust is visible at all latitudes, but brightest at latitudes slightly higher than the inclination of the particle orbits. The reason for this shift is that the bands are centered on the Sun and not the Earth; hence when viewed at $\epsilon = 90°$, their smaller distance from the Earth shifts their apparent position to higher latitude. Further, the geocentric latitude of the bands depends on the wavelength of observation. At shorter wavelengths, we see more emission from dust that is closer to the Earth. Migrating dust "passing overhead," seen along the line of sight toward the ecliptic pole, has the same spectrum as any other dust near the Earth's orbit; dust still near the production site is cooler, and can only be seen at relatively low latitudes ($<9\overset{\circ}{.}5$ in the example shown in Fig. 10).

5.3. *Comparison of the Model with the Observations*

The basic observational data on the bands derived in §§ 2–4 from the low-resolution *IRAS* data may be summarized as follows: The bands are broad (widths ~3°), and the peak brightness shifts to higher latitudes at shorter wavelengths (§ 2); the parallactic distance of the band material from the Sun is smaller than that of the asteroid belt (§ 3); and the color temperature of the band material is warmer than expected for dust in the asteroid belt but consistent with that expected for dust at the derived parallactic distance (§ 4).

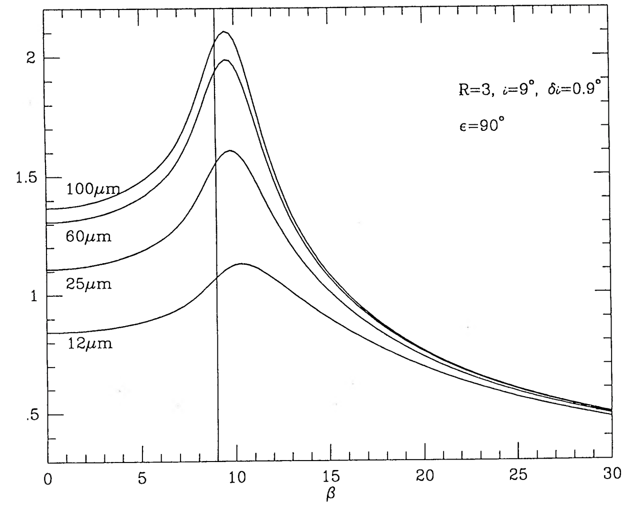

FIG. 10.—Model profiles of a "migrating" band created by particles that originate at $R = 3$ AU, with common inclination $i = 9°$ and dispersion $\delta i = 0.9°$. Each curve corresponds to the central wavelength of an *IRAS* (or *COBE*) filter, as labeled. The vertical axis is scaled as in the previous figure.

In order to use the migrating band model to explain the properties of the bands, we have generated models with a range of i, δi, and R, and analyzed them the same way the observations were analyzed. Model band profiles were computed between ecliptic latitudes $\pm 16°$ with a $0\overset{\circ}{.}25$ step size, and a fourth-order polynomial baseline similar to a typical *IRAS* scan was added. The profile was then decomposed into a pair of Gaussians and a fourth-order baseline using the same software as used to analyze the data (§ 2). The dependence of the Gaussian properties on the model parameters is generally straightforward: (1) the separation between the northern and southern components of a band pair is a measure of the mean orbital inclination of the band material; and (2) the width of a band is a measure of the dispersion in orbital inclinations. The radius of the band affects both of these properties in the same way (by increasing the widths and separations), but it cannot be measured from a single scan.

The observed separation and width of the outer bands are best fitted by a migrating band model with $i = 8\overset{\circ}{.}5$, $\delta i = 0\overset{\circ}{.}4$ for $R = 2.7$ AU. As noted above, the band radius cannot be determined from the widths and separations alone. For this, we simulated the parallax measurements (§ 3.2) by fitting model profiles with elongations $\epsilon = 80$, 90, and 100°. While the parallactic distance R_p (as derived in § 3.2) of a migrating band increases with R, the relationship between R_p and R is not quite linear; models with $R = 1.5$ to 3 AU give parallactic radii of $R_p = 1.5$ to 2.7 AU. The observed parallactic radius of the outer band pair was $R_p = 1.9$ AU, corresponding to a model with $R \simeq 2.0$ AU. The observed parallactic radius of the inner band pair was 1.8 AU, corresponding to a model with $R \simeq 1.9$ AU.

The straightforward relationships between model parameters and properties derived from fits to the profiles break down for low-inclination bands. The problem occurs when the separation between the northern and southern components of a band pair is less than the width (FWHM) of an individual component, so that the two components are severely blended. The central latitudes of the inner bands are well determined from the Gaussians, and these latitudes are best fitted by a migrating band model with $i = 1\overset{\circ}{.}1$. However, the widths and amplitudes of the separate Gaussians depend on the shape of the baseline. In particular, when the smooth zodiacal emission "baseline" peaks at a latitude that is more positive than the midplane of the bands, the southern component is found to be both wider and higher in amplitude than the northern component; some of the northern component brightness is evidently included in the polynomial baseline. This effect is evident in the data for the inner bands: the northern and southern band widths and amplitudes vary—out of phase—as the latitude of peak zodiacal emission varies. Thus we cannot fit the migrating band model to the inner bands in detail. Note that this is not a defect in the data, nor in the fitting procedures. The inner bands are known to be a blend of two separate band pairs, and it is likely that many bands with widths greater than their proper inclination are superposed to form a large fraction of the diffuse zodiacal emission (Sykes 1988). Low-inclination migrating bands cannot be cleanly separated from the smooth zodiacal emission because they *are* a large fraction of the zodiacal emission.

6. CONCLUSIONS

The material responsible for the zodiacal dust bands was created beyond 2.3 AU from the Sun and has migrated toward the Sun. From the variations of the band position as a function of longitude, the midplanes of the bands (i.e., their forced orbital elements) were deduced (Table 2). Orbits in the inner solar system are forced by Jovian gravity, and the forced inclination and node approach the Jovian values ($i_J = 1\overset{\circ}{.}3$, $\Omega_J = 100°$) for orbits with semimajor axis greater than ~ 3 AU; orbits with semimajor axis less than 2.3 AU have noticeably different forced elements (Dermott et al. 1985). If the band material were created in the asteroid belt and rapidly transported toward the Sun, the forced orbital elements would retain asteroidal values. On the other hand, if the transport were slow, the forced orbital elements would assume the values appropriate to a test particle resident at each heliocentric distance traversed. The time scale for Poynting-Robertson drag to change the orbital semimajor axis from a to 0 is $\tau_{\rm PR} \simeq 2 \times 10^3 a^2 s$ yr, where a is in AU and s is the particle radius in μm (Burns et al. 1979). The time scale from orbital element forcing by Jupiter is of the same order as the time scale for differential precession (Sykes & Greenberg 1986), and the ratio of Poynting-Robertson to differential-precession time scales is

$$\frac{\tau_{\rm PR}(a \to 0)}{\tau_{\rm prec}(a)} \sim \left(\frac{a}{3\ \rm AU}\right)^5 \left(\frac{v_{\rm ej}}{10^3\ \rm cm\ s^{-1}}\right)\left(\frac{s}{200\ \mu m}\right), \qquad (10)$$

where $v_{\rm ej}$ is the velocity dispersion of particles in the dust band. Under the catastrophic disruption hypothesis, $v_{\rm ej}$ represents the ejecta velocity from the asteroid disruption. Based on extrapolation from laboratory impact experiments (Fujiwara & Tsukamoto 1980) and the escape velocity from a 15 km asteroid, we estimate $10^2 < v_{\rm ej} < 10^4$ cm s^{-1}. Particles in the size range that dominates the infrared emission have comparable time scales for orbital changes due to radiation pressure and gravitational perturbation. The fact that the measured forced orbital elements of the broad bands differ from the forced orbital elements of dust near the Earth's orbit (Table 2), in the sense that the orbital elements of the band material are closer to those of asteroids and Jupiter, is indicative of its origin—beyond 2 AU from the Sun—and the rapid evolution of its orbital elements—due to Poynting-Robertson drag.

Using a migrating band model, we found that the observed properties of the outer bands could be explained by destruction of a parent body whose proper inclination is $i \simeq 8\overset{\circ}{.}5$. The dispersion in the inclinations of migrating band particles was found to be $\delta i \simeq 0\overset{\circ}{.}4$, shifting the latitude of peak emission to $8\overset{\circ}{.}3$ as observed. If the dispersion in inclinations were due solely to the kinetic energy imparted to the fragments when the parent body was destroyed, then we deduce that the dispersion in the distribution of ejecta speeds was $v_{\rm ej} \sim 10^4$ cm s^{-1} (for a parent body 3 AU from the Sun in a circular orbit). Since additional dispersion is likely to have been produced in subsequent collisions, we view this as an upper limit, in accord with the highest ejecta speeds mentioned above.

Future advances in understanding the connection between the zodiacal dust band will be possible through more realistic theoretical modeling of the evolution of asteroid collision remnants. The fact that parallactic distances determined on different dates appear significantly different (Fig. 6) implies that there may be both radial and azimuthal asymmetry in the distribution of interplanetary dust. The asymmetry could be due to particles that are rapidly transported (i.e., smaller than ~ 100 μm) from regions of enhanced collisional activity. Observationally, the Diffuse Infrared Background Experiment aboard the *Cosmic Background Explorer* (*COBE*) will produce superior low angular resolution spectrophotometric data on the bands, because the gain and background are accurately calibrated for *COBE* data (as opposed to the bootstrap calibration of extended emission required for *IRAS* data). It may be possible to discriminate material that has migrated from a discrete event in the asteroid belt using the different seasonal variations of the band brightness and latitude. It may also be possible to discriminate relatively cool dust in the asteroid belt from migrating dust by deconvolving the infrared background spectrum into multiple temperature components. If the spectrum is separated into temperature components for each independent observing direction, then the transition in morphology between dust in the asteroid belt and local dust should be evident. The migrating band model predicts that the bands will be evident at all heliocentric distances; whether multiple bands merge smoothly into the zodiacal cloud, or the cloud is morphologically distinct from the bands, remains to be discovered.

This paper is based on work supported in part by the National Science Foundation under award no. AST-8818544, and in part by a NASA (Astrophysics Data Program) grant to C. Heiles of the Berkeley Astronomy Department. The author thanks M. V. Sykes for valuable discussions before and after receiving this manuscript as referee.

REFERENCES

Boulanger, F., & Perault, M. 1988, ApJ, 330, 964
Brownlee, D. E. 1985, Ann. Rev. Earth Planet. Sci., 13, 147
Burns, J. A., Lamy, P. L., & Soter, S. 1979, Icarus, 40, 1
Ceplecha, Z. 1988, Bull. Astron. Inst. Czechoslovakia, 39, 221
Cleary, M. N., Haslam, C. G. T., & Heiles, C. 1979, A&AS, 36, 95
Davis, D. R., Chapman, C. R., Weidenschilling, S. J., & Greenberg, R. 1985, Icarus, 62, 30
Dermott, S. F., Nicholson, P. D., Burns, J. A., & Houck, J. R. 1984, Nature, 312, 505
———. 1985, in Properties and Interactions of Interplanetary Dust, ed. R. H. Giese & P. Lamy (Dordrecht: Reidel), 395
Dermott, S. F., Nicholson, P. D., Kim, Y., Wolven, B., & Tedesco, E. F. 1988, in Comets to Cosmology, ed. A. Lawrence (London: Springer), 3
Dohnanyi, J. S. 1970, J. Geophys. Res., 17, 3468
Fujiwara, A., & Tsukamoto, A. 1980, Icarus, 44, 142
Gradie, J. C., Chapman, C. R., & Williams, J. G. 1979, in Asteroids ed. T. Gehrels (Tucson: Univ. Arizona Press), 359
Grün, E., Zook, H. A., Fechtig, H., & Giese, R. H. 1985, Icarus, 62, 244
Hauser, M. G. 1988, in Comets to Cosmology, ed. A. Lawrence (London: Springer), 27
Hanner, M. S., Sparrow, J. G., Weinberg, J. L., & Beeson, D. E. 1976, in Zodiacal Light and Interplanetary Dust, ed. H. Elsässer & H. Fechtig, Lecture Notes Phys., 48, 29
Heiles, C., & Habing, H. J. 1974, A&AS, 14, 1
IRAS Catalogs and Atlases: Explanatory Supplement 1988, ed. C. A. Beichman, G. Neugebauer, H. J. Habing, P. E. Clegg, & T. J. Chester (Washington, DC: US Government Printing Office)
Leinert, C., Richter, I., Pitz, E., & Planck, N. 1981, A&A, 103, 177
Leinert, C., Röser, S., & Buitrago, J. 1983, A&A, 118, 345
Low, F., et al. 1984, ApJ, 278, L15
Maurette, M., Jéhanno, C., Robin, G., & Hammer, C. 1987, Nature, 328, 699
Mazets, E. P., et al. 1986, in Proc. 20th ESLAB Symposium on the Exploration of Halley's Comet, ed. B. Battrick, E. J. Rolfe, & R. Reinhard, ESA SP-250, 2, 3
McDonnell, J. A. M., et al. 1987, A&A, 187, 719
Reach, W. T. 1988, ApJ, 335, 468 (Paper I)

Reach, W. T. 1991a, ApJ, 369, 529 (Paper II)
———. 1991b, in Origin and Evolution of Interplanetary Dust, ed. A. C. Levasseur-Regourd, in press
Reach, W. T., & Heiles, C. 1988, in Comets to Cosmology, ed. A. Lawrence (London: Springer), 40
Sandford, S. A. 1986, Icarus, 68, 377
———. 1987, Fund. Cosmic Phys., 12, 1
Sekanina, Z., & Southworth, R. N. 1975, Physical and Dynamical Studies of Meteors: NASA CR-2615
Sykes, M. V. 1988, ApJ, 334, L55
———. 1990, Icarus, 84, 267
Sykes, M. V., & Greenberg, R. 1986, Icarus, 65, 51
Sykes, M. V., Greenberg, R., Dermott, S. F., Nicholson, P. D., Burns, J. P., & Gautier, T. N. 1989, in Asteroids II, ed. R. P. Binzel, T. Gehrels, & M. S. Matthews (Tucson: Univ. Arizona Press), 336
Sykes, M. V., Lebofsky, L. A., Hunten, D. M., & Low, F. J. 1986, Science, 232, 1115
Sykes, M. V., Lien, D. J., & Walker, R. G. 1990, Icarus, 86, 236
Sykes, M. V., & Walker, R. G. 1992, Icarus, in press
Wetherill, G. W., & Chapman, C. R. 1988, in Meteorites and the Early Solar System, ed. J. F. Kerridge & M. S. Matthews (Tucson: Univ. Arizona Press), 35
Wyatt, S. P., & Whipple, F. L. 1950, ApJ, 111, 134